Electronic Supplementary Information

Atomic-scale view of stability and degradation of single-crystal $MAPbBr_3$ surfaces

Joong Il Jake Choi[1], Muhammad Ejaz Khan[2,3], Zafer Hawash[4], Ki Jeong Kim[5], Hyunhwa Lee[1,5], Luis K. Ono[4], Yabing Qi[4], Yong-Hoon Kim[2,3]* and Jeong Young Park[1,3,6]**

[1]Center for Nanomaterials and Chemical Reactions, Institute for Basic Science (IBS), Daejeon 34141, Republic of Korea.

[2]School of Electrical Engineering, Korea Advanced Institute of Science and Technology (KAIST), Daejeon 34141, Republic of Korea.

[3]Graduate School of Energy, Environment, Water, and Sustainability, Korean Advanced Institute of Science and Technology (KAIST), Daejeon 34141, Republic of Korea.

[4]Energy Materials and Surface Sciences Unit (EMSSU), Okinawa Institute of Science and Technology Graduate University (OIST), 1919-1 Tancha, Onna-son, Kunigami-gun, Okinawa 904-0495, Japan.

[5]Beamline Research Division, Pohang Accelerator Laboratory (PAL), Pohang University of Science and Technology (POSTECH), Pohang, 37673, Korea

[6]Department of Chemistry, Korea Advanced Institute of Science and Technology (KAIST) Daejeon 34141, Republic of Korea.

Corresponding author contact:

Yabing.Qi@OIST.jp, y.h.kim@kaist.ac.kr, jeongypark@kaist.ac.kr.

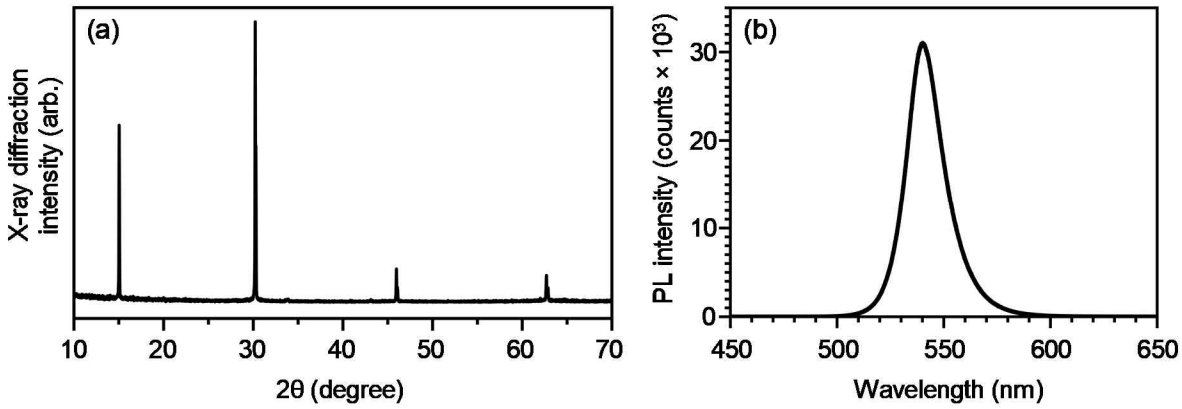

Figure S1. (a) X-ray diffraction (XRD) and (b) photoluminescence (PL) spectra of the $MAPbBr_3$ single crystal used in the current study. The measurement was conducted in ambient air; the sample was freshly cleaved before the measurements to minimize the effect of degradation in air. The excitation laser wavelength for the PL measurement was 325 nm.

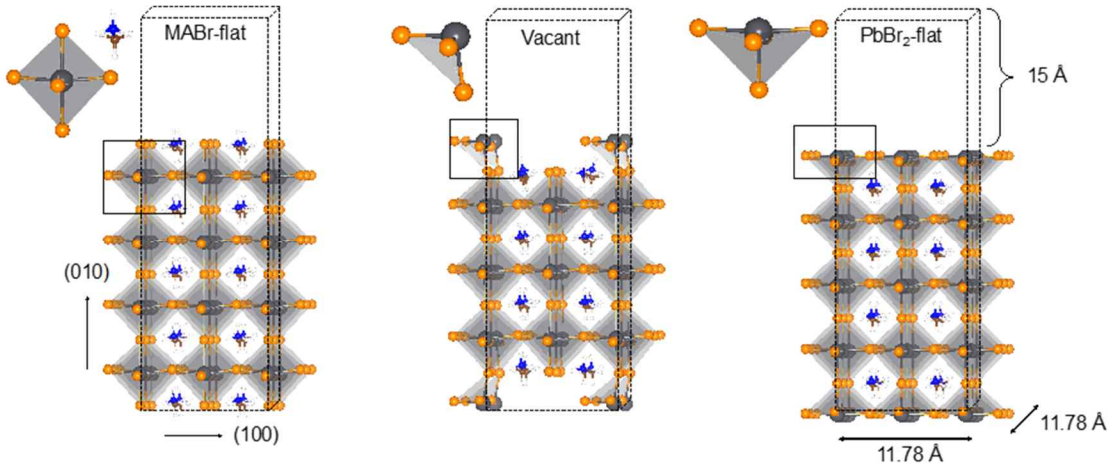

Figure S2. Optimized crystal structure of the $MAPbBr_3$ (001) surface terminations. A few selected simulation supercells for the different $MAPbBr_3$ surfaces considered in this work. The dotted black boxes indicate the unit cell for each case with a 15 Å vacuum region inserted perpendicular to the surface. The outermost $PbBr_x$ polyhedrons for these surfaces are shown in the insets. Two similar surface morphologies, Vacant and Vacant', have the difference of just one $PbBr_2$ molecule in the topmost atomic layer (see Figure 3).

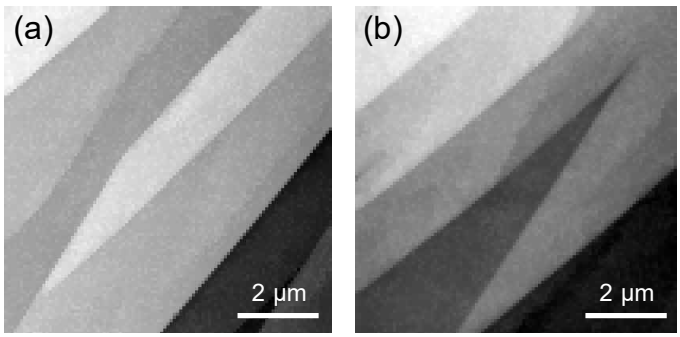

Figure S3. Large (8μm × 8μm) AFM topography images of two areas of a freshly cleaved $MAPbBr_3$ single crystal showing large terraces. The clear steps shown in the images are several nanometers in size.

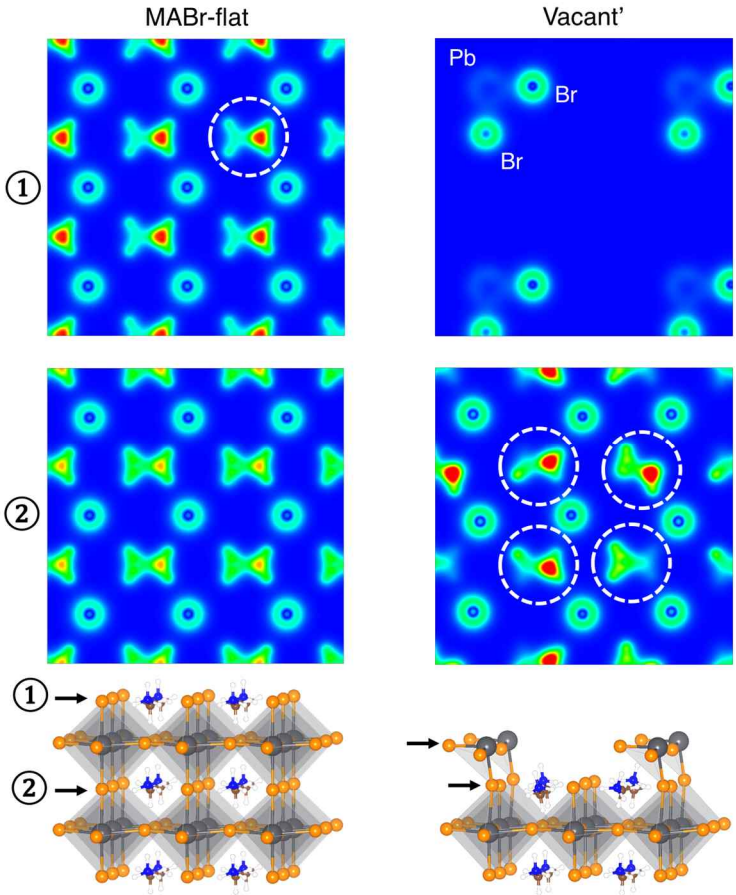

Figure S4. Contour plots for the charge planes cut at the topmost surface and at the second layer of the $MAPbBr_3$ perovskite. Electronic state distribution around the outermost region of the MABr-flat and Vacant' (001) surfaces are shown in the left and right panels, respectively. The corresponding surface atomic models are also included in the bottom panels, where the black arrows indicate the positions of the cut planes in the contour plots. The distorted (tilted or rotated *etc.*) ligands with respect to their fellow ligands in the bulk region are marked with dotted white circles.

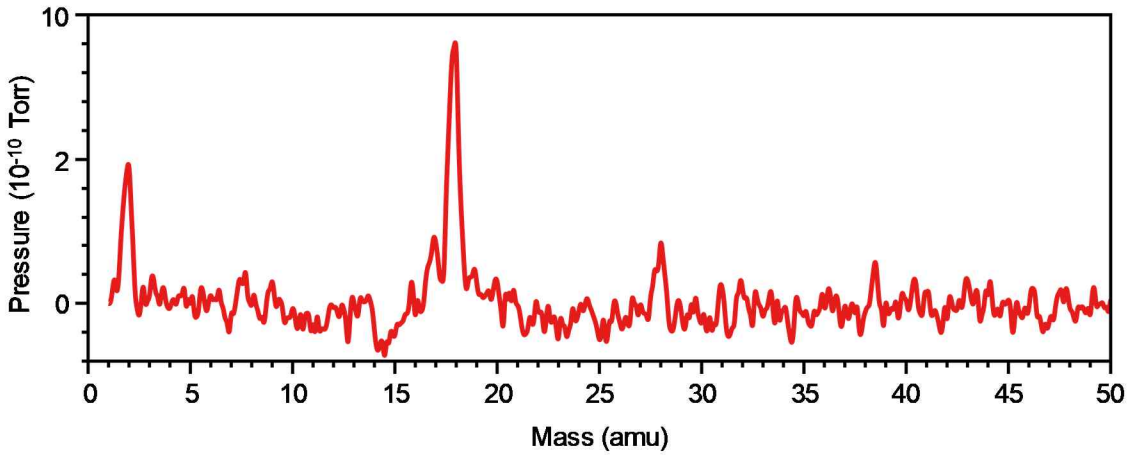

Figure S5. Residual gas analysis of the UHV chamber in which all AFM measurements took place. The analysis was performed using a quadrupole mass spectrometer. The notable peaks can be designated as hydrogen (2 amu), water (18 amu), and carbon monoxide (28 amu). Relatively high water and hydrogen contamination of the chamber could be the degradation source for the $MAPbBr_3$ by dissociation at the hot filament of the ion pressure gauge or at the ionization pump in the chamber.

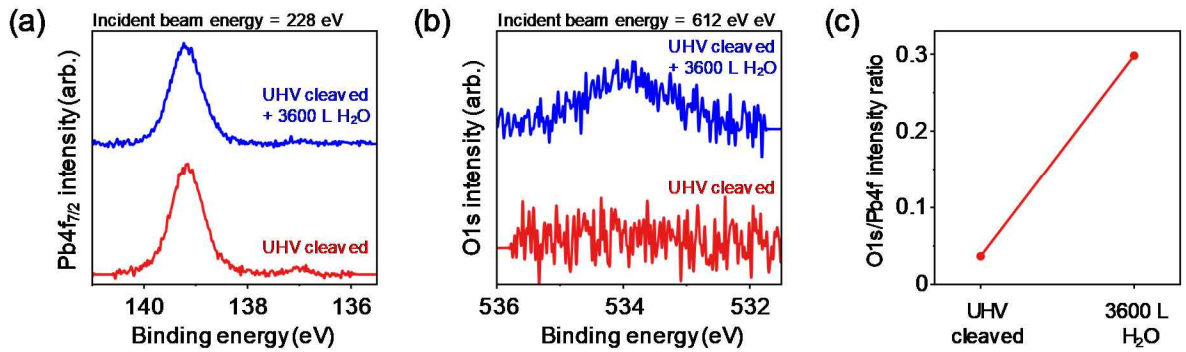

Figure S6. XPS spectra of (a) Pb4f and (b) O1s peaks from UHV-cleaved $MAPbBr_3$ (red) and after exposure to 10^{-6} mbar of water for 60 minutes (blue). The incident beam energy was chosen to obtain all spectra from comparable probing depths at a photoelectron kinetic energy of ≈ 90 eV. (c) O1s/Pb4f intensity ratio from (a) and (b).

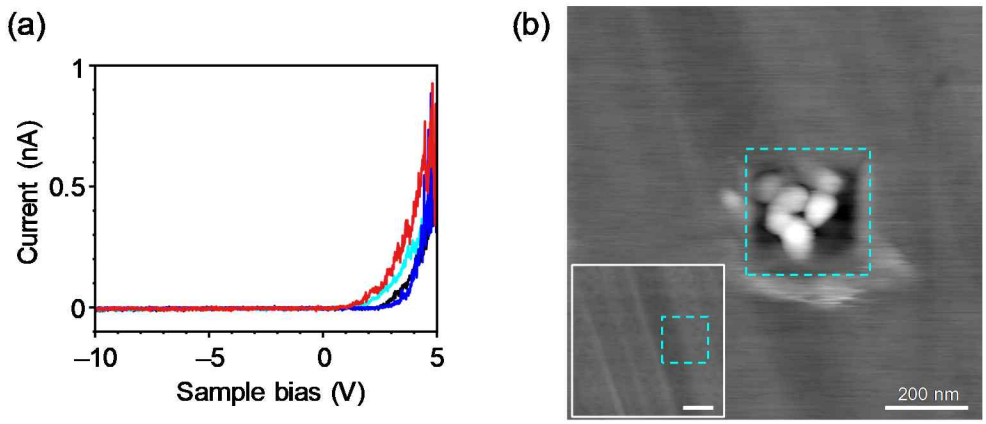

Figure S7. Details of the I–V measurements. (a) Individual I–V curves for the I–V curve presented in Figure 4(b). (b) Surface morphologies before (inset) and after contact-mode AFM scans with the various applied biases in Figure 4(a). Scale bars are 200 nm.

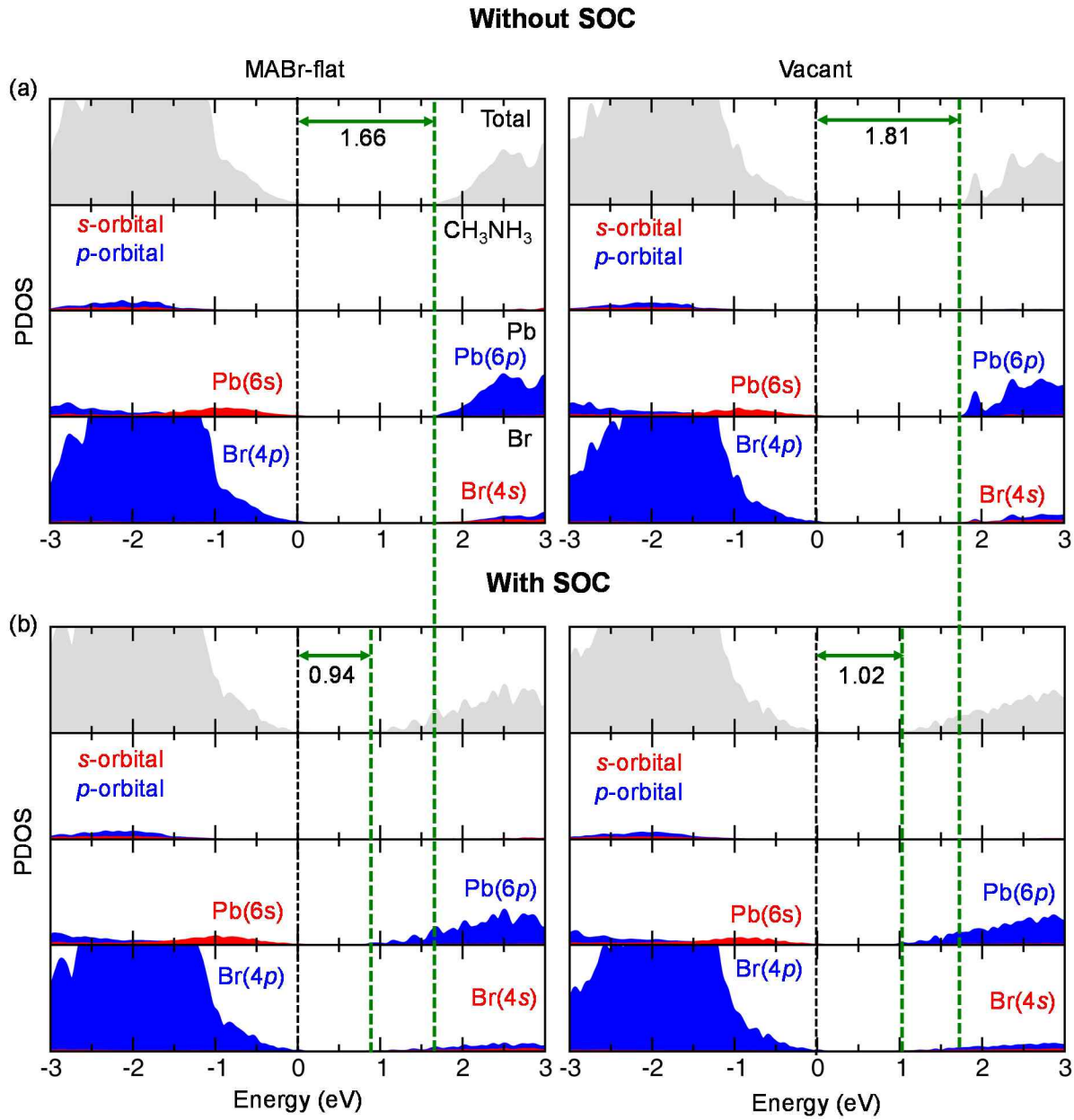

Figure S8. Spin-orbit coupling effect in the electronic structure. PDOS analysis showing the orbital contribution of two stable $MAPbBr_3$ surfaces. (a) PBEsol and (b) PBEsol-SOC results are compared, where downshifting of the states at the bottom conduction band edge region is noticeable.

Computation method for the stability of non-polar surfaces

The stability of non-polar surfaces was determined by calculating their formation energies according to

$$\Delta\Omega = \frac{1}{2A_S}(E_S - N_S E_B/N_B)\,, \tag{S1}$$

where E_B and E_S are the total DFT energies of the relaxed $MAPbBr_3$ bulk and slab structural forms, respectively, N_B and N_S are the number of atoms in the bulk unit cell and slab supercell models, respectively, and A_S is the surface area of the slab.

Computation method for the grand potential

The grand potential for determining the phase diagram of the structural stability was calculated according to

$$\begin{aligned}\Theta\left(\Delta\mu_{\mathrm{MA}},\Delta\mu_{\mathrm{Pb}},\Delta\mu_{\mathrm{Br}},\Delta\mu_{\mathrm{MAPbBr_3}}\right)&\\ \approx E_S\left[\mathrm{MA}_\alpha\mathrm{Pb}_\beta\mathrm{Br}_\gamma(\mathrm{MAPbBr_3})_\chi\right]-\alpha\mu_{\mathrm{MA}}^{\mathrm{solid,bcc}}&\\ -\beta\mu_{\mathrm{Pb}}^{metal}-\frac{\gamma}{2}\mu_{\mathrm{Br_2}}^{\mathrm{gas}}-\chi\mu_{\mathrm{MAPbBr_3}}^{\mathrm{cubic}}-\alpha\Delta\mu_{\mathrm{MA}}-\beta\Delta\mu_{\mathrm{Pb}}&\\ -\gamma\Delta\mu_{\mathrm{Br}}-\chi\Delta\mu_{\mathrm{MAPbBr_3}},&\end{aligned} \tag{S2}$$

$$\begin{aligned}\Delta\mu_{\mathrm{MA}}=\mu_{\mathrm{MA}}-\mu_{\mathrm{MA}}^{\mathrm{solid,bcc}},\quad \Delta\mu_{\mathrm{Pb}}=\mu_{\mathrm{Pb}}-\mu_{\mathrm{Pb}}^{metal},&\\ \Delta\mu_{\mathrm{Br}}=\mu_{\mathrm{Br}}-\frac{1}{2}\mu_{\mathrm{Br_2}}^{\mathrm{gas}},\quad \Delta\mu_{\mathrm{MAPbBr_3}}=\mu_{\mathrm{MAPbBr_3}}-\mu_{\mathrm{MAPbBr_3}}^{\mathrm{cubic}}.&\end{aligned} \tag{S3}$$

where E_S is the total energy of the fully relaxed slab consisting of α MA ligands, β Pb atoms, γ Br atoms, and χ $MAPbBr_3$ complexes. μ_i is the chemical potential of component *i*. $\mu_{\mathrm{MA}}^{\mathrm{solid,bcc}}$, $\mu_{\mathrm{Pb}}^{metal}$, $\mu_{\mathrm{Br_2}}^{\mathrm{gas}}$, and $\mu_{\mathrm{MAPbBr_3}}^{\mathrm{cubic}}$ are the chemical potentials of the body centered cubic phase of MA following the solid Cs configuration,[1] Pb bulk, Br_2 gas, and $MAPbBr_3$ cubic bulk phases, respectively, calculated using the DFT approach. We ignored the entropy term in eq. (S2), which follows the conventional DFT studies of surfaces.[2,3]

Hybrid halide perovskite surface degradation process

To further investigate the surface degradation process at the MABr-, Br_2- and $PbBr_2$-rich and poor conditions, we computed the MA, CH_3NH_2, and HBr desorption energies ($E_d = \sum E_{products} - \sum E_{reactants}$) using

$$E_d^{MA} = \frac{1}{n_{MA}}\left[\left(E_{Br-flat} + n_{MA}\mu_{MA}\right) - E_{MABr-flat}\right], \quad \text{(S4)}$$

$$E_d^{CH_3NH_2} = \frac{1}{n_{CH_3NH_2}}\left[\left(E_{HBr-flat} + n_{CH_3NH_2}\mu_{CH_3NH_2}\right) - E_{MABr-flat}\right], \quad \text{(S5)}$$

$$E_d^{HBr} = \frac{1}{n_{HBr}}\left[\left(E_{PbBr_2-flat} + n_{HBr}\mu_{HBr}\right) - E_{HBr-flat}\right], \quad \text{(S6)}$$

where equations (S4)–(S6) include the DFT energies of the reactants and product surfaces as well as their desorbed components. In addition to the desorption energies of the gases, we also calculated the dissociative binding energy for the $PbBr_2$ species using

$$E_d^{PbBr_2} = \frac{1}{n_{PbBr_2}}\left[\left(E_{vacant} + n_{PbBr_2}\mu_{PbBr_2}\right) - E_{PbBr_2-flat}\right], \quad \text{(S7)}$$

where μ_{PbBr_2} is the energy of the $PbBr_2$ molecule obtained from its bulk unit cell calculation. The calculated desorption energies of those molecules are presented in Table S4.

Table S1. The optimized lattice constants of $MAPbBr_3$ for the bulk and slab structures. Experimental lattice parameters from the literature.[4]

	Bulk		Slab	
Exp.	PBEsol	DFT-D3	PBEsol	DFT-D3
5.90	5.93	5.89	5.89	5.87

Table S2. The surface formation energy calculated using PBEsol and DFT-D3 for the selected model structures. We determined the surface stability for the $MAPbBr_3$ cleaved at the (001) termination by calculating the surface formation energy. The PBEsol results are compared with the van der Waals corrected DFT-D3 values and we find that those remain very similar to each other, which may result from the similar lattice parameters (see Table S1) calculated in both approaches.

Surface Type	Surface Energy [meV/Å^2 (J/m^2)]	
	PBEsol	DFT-D3
MABr-flat	−39.91 (−0.64)	−29.32 (−0.47)
Vacant′	−13.89 (−0.22)	−9.06 (−0.14)
Vacant	5.04 (0.08)	18.10 (0.29)
$PbBr_2$-flat	55.99 (0.90)	52.24 (0.84)
HBr-flat	155.82 (2.50)	158.73 (2.54)

Table S3. Details of the stable $MAPbBr_3$ surface models for the grand potential computation.

Termination label	Composition ratio	Number of atoms
MABr-flat	$MA_4Br_4(MAPbBr_3)_{16}$	228
Vacant′	$MA_2Br_2(MAPbBr_3)_{14}$	186
Vacant	$(MAPbBr_3)_{16}$	192
$PbBr_2$-flat	$Pb_4Br_8(MAPbBr_3)_{16}$	204

Table S4. Desorption energy E_d [eV] calculated within DFT using PBEsol and DFT-D3 for the MA ligands and molecules adsorbed at the $MAPbBr_3$ surface.

Molecule	Desorption Energy [eV]	
	PBEsol	DFT-D3
MA	4.22	4.38
CH_3NH_2	2.33	2.63
Br_2/Br^-	0.11	0.11
$PbBr_2$	0.10	0.28

Reference

1 W.-J. Yin, T. Shi and Y. Yan, *Appl. Phys. Lett.*, 2014, **104**, 063903.
2 G.-X. Qian, R. M. Martin and D. J. Chadi, *Phys. Rev. Lett.*, 1988, **60**, 1962–1965.
3 J. Haruyama, K. Sodeyama, L. Han and Y. Tateyama, *J. Phys. Chem. Lett.*, 2014, **5**, 2903–2909.
4 A. Poglitsch and D. Weber, *J. Chem. Phys.*, 1987, **87**, 6373–6378.